Growth of Black Holes and Their Host Spheroids in (Sub)mm-loud High-Redshift QSOs *

Cai-Na Hao[1,2,3], Xiao-Yang Xia[1], Shu-De Mao[4], Zu-Gan Deng[5] and Hong Wu[2]

[1] Tianjin Astrophysics Center, Tianjin Normal University, Tianjin 300384; *hcn@ast.cam.ac.uk*
[2] National Astronomical Observatories, Chinese Academy of Sciences, Beijing 100012
[3] Institute of Astronomy, University of Cambridge, Madingley Road, Cambridge CB3 0HA, UK
[4] Jodrell Bank Observatory, University of Manchester, Macclesfield, Cheshire SK11 9DL, UK
[5] Graduate School of Chinese Academy of Sciences, Beijing 100049

Abstract We study the growth of black holes and stellar population in spheroids at high redshift using several (sub)mm-loud QSO samples. Applying the same criteria established in an earlier work, we find that, similar to IR QSOs at low redshift, the far-infrared emission of these (sub)mm-loud QSOs mainly originates from dust heated by starbursts. By combining low-z IR QSOs and high-z (sub)mm-loud QSOs, we find a trend that the star formation rate ($\dot{M}_\star$) increases with the accretion rate ($\dot{M}_{\rm acc}$). We compare the values of $\dot{M}_\star/\dot{M}_{\rm acc}$ for submm emitting galaxies (SMGs), far-infrared ultraluminous/hyperluminous QSOs and typical QSOs, and construct a likely evolution scenario for these objects. The (sub)mm-loud QSO transition phase has both high $\dot{M}_{\rm acc}$ and $\dot{M}_\star$ and hence is important for establishing the correlation between the masses of black holes and spheroids.

Key words: galaxies: active — galaxies: evolution — galaxies: high-redshift — galaxies: interactions — quasars: general — galaxies: starburst

1 INTRODUCTION

In the last few years, it has become increasingly clear that the growth of supermassive black holes must be closely related to the growth of their host spheroids, as the black hole mass is correlated with the galactic velocity dispersion (e.g., Ferrarese & Merritt 2000; Tremaine et al. 2002) and the luminosity/mass of the hot stellar component of the host galaxy (e.g., Magorrian et al. 1998; Laor 1998; Kormendy & Gebhardt 2001). However, it remains unclear how the correlations arise. Although much efforts have been made both theoretically (e.g. Silk & Rees 1998; Haehnelt & Kauffmann 2000; Adams et al. 2001; Burkert & Silk 2001; Balberg & Shapiro 2002; Springel et al. 2005; Di Matteo et al. 2005) and observationally (e.g. Shields et al. 2003; Treu et al. 2004; Heckman et al. 2004; Walter et al. 2004; Borys et al. 2005, Shields et al. 2006), a definitive interpretation still remains to be established.

In an earlier work, Hao et al. (2005, hereafter Paper I) studied QSOs/Seyfert 1s selected from local ultraluminous infrared galaxies (IR QSOs) and found a correlation between the star formation rate ($\dot{M}_\star$) and the accretion rate to the central AGNs ($\dot{M}_{\rm acc}$), with the ratio of $\dot{M}_\star$ to $\dot{M}_{\rm acc}$ at about several hundred (Paper I). These IR QSOs not only have massive starbursts occurring in their host galaxies their optical spectroscopic and X-ray properties also exhibit characteristics of young forming QSOs (Zheng et al. 2002). Thus IR QSOs may be an important evolution phase from massive starbursts to luminous QSOs and later to elliptical galaxies. During this transition phase, both the spheroid component and central black hole grow

rapidly. Therefore, it is important to extend our previous studies of the local universe to high redshift in order to better understand how the correlation between the masses of spheroids and their central black holes arises and evolves in time.

Massive submillimeter-emitting galaxies (SMGs), uncovered by deep SCUBA surveys on blank fields, resemble scaled-up versions of the local ultraluminous infrared galaxies at high redshift (e.g. Tacconi et al. 2006) – their star formation rates and molecular gas reservoirs are one order of magnitude higher (on average) than their counterparts at low redshift (e.g. Kim et al. 1998; Downes & Solomon 1998; Chapman et al. 2004; Alexander et al. 2005b). In addition, recent investigations on the SMGs by ultra-deep X-ray observations (the 2 Ms Chandra Deep Field North) have revealed only modest $\dot{M}_{\rm acc} \lesssim 1 M_\odot \, {\rm yr}^{-1}$ for their central AGNs (Alexander et al. 2005a,b). These observations indicate that the current SMG samples contain few luminous QSOs, so they are not ideal samples from which we can identify high-z analogues of local IR QSOs. On the other hand, targeted observations of high-z QSOs at submillimeter (submm) wavelengths reveal a category of submm-loud QSOs (e.g., McMahon et al. 1999; Isaak et al. 2002). The average redshift and submm flux density of these submm-detected QSOs by Stevens et al. (2005) are consistent with the SMGs, but their median X-ray flux is 30 times higher than those of the SMGs selected from blank fields, indicating much higher $\dot{M}_{\rm acc}$ values than those of the SMGs (see also Alexander et al. 2005b). Similarly, the average redshift and submm flux density of the submm-detected bright QSOs by Priddey et al. (2003a) are also comparable to those of the X-ray selected QSOs by Stevens et al. (2005). Note also that most of the submm-loud QSOs by Isaak et al. (2002) have also been detected at $1.2 \, {\rm mm}$ by Omont et al. (2001).

Given that several groups have investigated the properties of high-z bright QSO samples using targeted (sub)mm observations (e.g. Carilli et al. 2001; Omont et al. 2001, 2003; Priddey et al. 2003a,b; Stevens et al. 2005), it is natural to search from these samples for the high-z analogues of the local IR QSOs, and investigate their physical properties. We are particularly interested in how star formation and accretion are related to each other in the extreme environments and which of these two dominates the heating of dust that gives rise to the rest-frame (thermal) submm emissions (e.g., Carilli et al. 2001; Isaak et al. 2002). To achieve this, we extend the technique developed in Paper I to the high-z (sub)mm observed QSO samples. This paper is structured as follows. In Section 2, we describe how the samples are compiled. In Section 3, we discuss how the physical parameters are estimated. The main results are presented and discussed in Section 4. Finally, in Section 5, we summarize our results. Throughout this paper we adopt a cosmology with a matter density parameter $\Omega_{\rm m} = 0.3$, a cosmological constant $\Omega_\Lambda = 0.7$ and a Hubble constant of $H_0 = 70 \, {\rm km \, s^{-1} Mpc^{-1}}$.

2 SAMPLES

As discussed above, high-z QSO samples with submm or mm observations are needed for our purpose. First we collect several high-z, optically-selected QSO samples with mm ($1.2 \, {\rm mm}$) observations, taken from Carilli et al. (2001) and Omont et al. (2001, 2003). The $1.2 \, {\rm mm}$ observations made use of the Max-Planck Millimeter Bolometer (MAMBO; Kreysa et al. 1998) on the IRAM 30 m telescope on Pico Veleta in Spain. The details are given below. Note that the B-band absolute magnitudes (M_B) in the following descriptions are taken directly from the cited papers, appropriate for a cosmology with $H_0 = 50 \, {\rm km \, s^{-1} Mpc^{-1}}, \Omega_{\rm m} = 1$ and $\Omega_\Lambda = 0$.

(1) A QSO sample taken from Carilli et al. (2001) consists of 41 sources, which were found in the Sloan Digital Sky Survey (SDSS). They span a range of $M_{\rm B} = -26.1$ to -28.8 and a redshift range from $z = 3.6$ to 5.0. Of the 41 objects in the sample, 16 have $1.2 \, {\rm mm}$ flux densities 3 times greater than the rms noise (3σ).

(2) A QSO sample taken from Omont et al. (2001) consists of 65 objects, which were selected from Palomar Sky Survey (PSS). They have $M_{\rm B} < -27.0$ and $3.9 < z < 4.5$. Twenty one out of these 65 objects have flux densities greater than 3σ at $1.2 \, {\rm mm}$.

(3) An optically luminous ($M_{\rm B} < -27.0$) but radio quiet QSO sample taken from Omont et al. (2003) consists of 35 objects with redshifts $1.8 < z < 2.8$. Nine were detected at $1.2 \, {\rm mm}$ with flux densities $\geq 3\sigma$.

As the Submillimeter Common User Bolometer Array (SCUBA) detector on the JCMT has similar capabilities to MAMBO, we also collected high-z optically selected QSO samples observed at submm ($850\,\mu$m), taken from McMahon et al. (1999), Isaak et al. (2002) and Priddey et al. (2003a,b):

(1) An optically luminous ($M_{\rm B} < -27$) and radio quiet QSO sample from McMahon et al. (1999) with redshifts $z \gtrsim 4$. Seven out of the 10 QSOs were detected at levels $\geq 3\sigma$ at $850\,\mu$m.
(2) An optically luminous ($M_{\rm B} < -27.5$) and radio quiet QSO sample from Isaak et al. (2002) consists of 38 objects with redshift $z \geq 4$. Eight were detected at $850\,\mu$m with flux densities at levels $\geq 3\sigma$.
(3) An optically luminous ($M_{\rm B} < -27.5$) and radio quiet QSO sample taken from Priddey et al. (2003a) consists of 57 objects with redshifts $1.5 < z < 3.0$. Nine were detected at $850\,\mu$m with flux densities at levels $\geq 3\sigma$.
(4) An optically selected QSO sample with redshifts > 4.9 from Priddey et al. (2003b) consists of 14 objects, among which four were detected at $850\,\mu$m at $\geq 4\sigma$ levels (see Priddey et al. 2003b for details).

In the following, we denote high-z sources as detected (non-detected) at $1.2\,$mm or at $850\,\mu$m if their flux densities are above (below) three times the rms noise level.

Besides these mm ($1.2\,$mm) and submm ($850\,\mu$m) observed high-z QSOs samples, we also collected high-z QSOs with ultraluminous or hyperluminous FIR luminosities ($> 10^{12}$ or $10^{13} L_\odot$) detected by other means, to verify the assumption in our method, because many of them have their infrared emissions unambiguously dominated by starbursts (see Sect. 4.1 of this paper; Stevens et al. 2005; Carilli et al. 2005). Specifically we include: (1) Nineteen X-ray absorbed, Compton-thin QSOs with submm (450 and $850\,\mu$m) photometry (Stevens et al. 2005), among which eight were detected at $850\,\mu$m. For comparison, there are observed 19 X-ray unabsorbed QSOs with non-detected at submm ($850\,\mu$m, Page et al. 2004). The submm photometry observations at 450 and $850\,\mu$m for these QSOs were performed using SCUBA. The redshift range of this sample is $1 < z < 3$. Note that two of the X-ray absorbed, Compton thin QSOs treated as detections had $2 < S/N < 3$ according to Stevens et al. (2005). (2) Two high-z QSOs (B1202$-$0725 and J1148+5251) with HCN and CO observations (Carilli et al. 2002; Walter et al. 2003; Isaak et al. 2004; Carilli et al. 2005) and one (B1335$-$0417) with only CO detections (Carilli et al. 2002). The B-band absolute luminosity and $1.25\,$mm flux densities for B1202$-$0725 and B1335$-$0417 were adopted from Omont et al. (1996); for J1148+5251, they were respectively taken from Robson et al. (2004) and Bertoldi et al. (2003). The comparison samples at low redshift are taken from Paper I. Briefly, these include an IR QSO sample, an optically selected Palomar-Green QSO (PG QSO) sample, and a narrow-line Seyfert 1 galaxy (NLS1) sample. IR luminosities and bolometric luminosities are available for all these objects (see Paper I for details).

As described above, most target QSOs were compiled from heterogeneous flux-limited samples, so they likely suffer from some selection biases. For example, QSOs at the bright end of the luminosity function (with high $\dot{M}_{\rm acc}$) are favored in our samples. Nevertheless, the selection of high $\dot{M}_{\rm acc}$ objects will not significantly impact on our results as our main purpose is to compare the relative growth of the black holes and spheroids (i.e., the ratio of $\dot{M}_\star$ and $\dot{M}_{\rm acc}$). We will return to this point in Section 4.2.

3 ESTIMATION OF PHYSICAL PARAMETERS

For the local sample, the values of various physical parameters except the star formation rate (see Sect. 3.2) were taken directly from Paper I, we refer readers to that paper for details. Below we discuss how to derive the physical parameters for the high-z objects. The values are listed in Tables 1 and 3 for the mm and submm detected QSOs, respectively.

3.1 Accretion Rates

The accretion rates are derived from the bolometric luminosities according to the formula given in Paper I:

$$\dot{M}_{\rm acc} = 6.74\, M_\odot\,{\rm yr}^{-1}\, \frac{L_{\rm bol}}{10^{13} L_\odot}. \tag{1}$$

For the objects not selected from X-ray observations, the bolometric luminosities were estimated from the absolute B-band magnitude converted to our adopted cosmology. A bolometric correction factor of

Table 1 Physical Parameters for the 1.2 mm Detected QSOs

Name	Redshift	$S_{1.2\mathrm{mm}}$	$\log(\frac{L_{\mathrm{bol}}}{L_\odot})$	$\log(\frac{L_{60\mu\mathrm{m}}}{L_\odot})$	$\log(\frac{\dot{M}_{\mathrm{acc}}}{M_\odot\,\mathrm{yr}^{-1}})$	$\log(\frac{\dot{M}_\star}{M_\odot\,\mathrm{yr}^{-1}})$	$\log(\frac{\dot{M}_\star}{\dot{M}_{\mathrm{acc}}})$
(1)	(2)	(3)	(4)	(5)	(6)	(7)	(8)
			Carilli et al. (2001)				
J012403.78+004432.7	3.81	2.0±0.3	14.272	12.884	2.101	3.089	0.988
J015048.83+004126.2	3.67	2.2±0.4	14.094	12.939	1.923	3.283	1.360
J023231.40−000010.7	3.81	1.8±0.3	13.612	12.838	1.441	3.271	1.830
J025112.44−005208.2	3.78	2.4±0.6	13.691	12.966	1.520	3.411	1.891
J025518.58+004847.6	3.97	2.1±0.4	14.066	12.890	1.895	3.220	1.325
J032608.12−003340.2	4.16	1.5±0.4	13.885	12.726	1.714	3.045	1.331
J033829.31+002156.3	5.00	3.7±0.3	13.634	13.050	1.463	3.514	2.051
J111246.30+004957.5	3.92	2.7±0.5	13.997	13.004	1.826	3.402	1.576
J122600.68+005923.6	4.25	1.4±0.4	13.946	12.688	1.775	2.950	1.175
J123503.04−000331.8	4.69	1.6±0.4	13.523	12.709	1.352	3.129	1.777
J141205.78−010152.6	3.73	4.5±0.7	13.759	13.244	1.588	3.718	2.130
J141332.35−004909.7	4.14	2.5±0.5	13.840	12.950	1.669	3.367	1.698
J142647.82+002740.4	3.69	3.9±0.8	13.670	13.186	1.499	3.661	2.162
J144758.46−005055.4	3.80	5.4±0.8	13.644	13.316	1.473	3.803	2.330
J161926.87−011825.2	3.84	2.3±0.6	13.612	12.942	1.441	3.393	1.952
J235718.35+004350.4	4.34	1.8±0.6	13.639	12.789	1.468	3.206	1.738
			Omont et al. (2001)				
PSSJ0209+0517	4.18	3.3±0.6	14.241	13.067	2.070	3.416	1.346
PSSJ0439−0207	4.40	2.3±0.7	14.003	12.891	1.832	3.246	1.414
PSSJ0808+5215	4.44	6.6±0.6	14.484	13.345	2.313	3.728	1.415
PSSJ1048+4407	4.40	4.6±0.4	13.963	13.192	1.792	3.639	1.847
PSSJ1057+4555	4.12	4.9±0.7	14.520	13.244	2.349	3.571	1.222
BRB1117−1329	3.96	4.1±0.7	14.278	13.181	2.107	3.564	1.457
BRB1144−0723	4.15	6.0±0.7	14.080	13.329	1.909	3.783	1.874
PSSJ1226+0950	4.34	2.8±0.7	13.963	12.981	1.792	3.380	1.588
PSSJ1248+3110	4.32	6.3±0.8	14.043	13.335	1.872	3.794	1.922
PSSJ1253−0228	4.00	5.5±0.8	13.878	13.305	1.707	3.775	2.068
PSSJ1317+3531	4.36	3.7±1.1	14.003	13.100	1.832	3.522	1.690
PSSJ1347+4956	4.56	5.7±0.7	14.325	13.271	2.154	3.671	1.517
PSSJ1403+4126	3.85	1.5±0.5	13.716	12.755	1.545	3.145	1.600
PSSJ1418+4449	4.32	6.3±0.7	14.443	13.335	2.272	3.726	1.454
PSSJ1535+2943	3.99	1.9±0.6	13.838	12.844	1.667	3.231	1.564
PSSJ1554+1835	3.99	6.7±1.1	13.638	13.392	1.467	3.883	2.416
PSSJ1555+2003	4.22	3.1±0.6	13.961	13.036	1.790	3.451	1.661
PSSJ1646+5514	4.04	4.6±1.5	14.479	13.224	2.308	3.557	1.249
PSSJ1745+6846	4.13	2.5±0.7	13.800	12.951	1.629	3.376	1.747
PSSJ1802+5616	4.16	2.8±0.9	13.761	12.997	1.590	3.438	1.848
PSSJ2322+1944	4.11	9.6±0.5	14.240	13.537	2.069	4.001	1.932
			Omont et al. (2003)				
KUV08086+4037	1.78	4.3±0.8	13.739	13.443	1.568	3.933	2.365
093750.9+730206[a]	2.52	3.8±0.9	14.368	13.304	2.197	3.704	1.507
HS1002+4400	2.08	4.2±0.8	14.273	13.400	2.102	3.840	1.738
HS1049+4033	2.15	3.2±0.7	14.235	13.273	2.064	3.693	1.629
110610.8+640008[a]	2.19	3.9±1.1	14.677	13.355	2.506	3.674	1.168
140955.5+562827[a]	2.56	10.7±0.6	14.329	13.749	2.158	4.227	2.069
154359.3+535903[a]	2.37	3.8±1.1	14.283	13.322	2.112	3.744	1.632
HS1611+4719	2.35	4.6±0.7	14.043	13.408	1.872	3.875	2.003
164914.9+530316[b]	2.26	4.6±0.8	14.240	13.418	2.069	3.866	1.797
			High-z optically faint QSO				
030117+002025[c]	5.5	0.87±0.20	12.374	12.387	0.216	2.878	2.662
			High-z QSOs with HCN/ CO obs.				
BRI1202−0725	4.693	12.59±2.28	14.407	13.657	2.236	4.120	1.884
BRI1335−0417	4.407	10.26±1.04	13.924	13.592	1.753	4.082	2.329
J1148+5251	6.419	5.0±0.6	14.388	13.095	2.217	3.396	1.179

Notes: Columns: (1) name. (2) redshift. (3) the observed flux density at 1.2 mm. (4) bolometric luminosity of AGN. (5) monochromatic luminosity at 60 μm (νL_ν) (6) accretion rate of central supermassive black hole in $M_\odot\,\mathrm{yr}^{-1}$. (7) star formation rate in $M_\odot\,\mathrm{yr}^{-1}$. (8) the ratio of the star formation rate to the accretion rate. The objects from different samples are separated and labeled. [a] The name with prefix [VV96]J. [b] The name with prefix [VV2000]J. [c] The name with prefix RDJ.

Table 2 Binned Data for 1.2mm Non-Detected QSOs

Number	mean redshift	weighted mean $S_{1.2\mathrm{mm}}$	weighted mean $\log(\frac{L_{\mathrm{bol}}}{L_{\odot}})$	weighted mean $\log(\frac{L_{60\mu\mathrm{m}}}{L_{\odot}})$
		Carilli et al. (2001)		
9	3.749	0.190±0.146	13.915	11.868±0.333
7	4.244	0.092±0.146	13.860	11.506±0.689
9	4.744	0.187±0.125	13.821	11.773±0.290
		Omont et al. (2001)[a]		
44	4.232	0.385±0.128	14.252	12.129±0.144
		Omont et al. (2003)		
19	2.172	0.672±0.210	14.219	12.593±0.136
7	2.529	0.738±0.287	14.074	12.592±0.169

Notes: The binned data for the 1.2mm non-detected QSOs in Carilli et al. (2001) and Omont et al. (2001, 2003). Columns: (1) The number of objects in each redshift bin with a bin width of 0.5. (2) The mean redshift in each bin. (3) The weighted mean flux density at $1.2\,\mathrm{mm}$. (4) The average bolometric luminosity in each bin. (5) The weighted mean of the monochromatic luminosity at $60\,\mu\mathrm{m}$.
[a] The redshift bin width is 0.56, which is the whole redshift range of this sample.

9.74 was adopted following Vestergaard (2004). For the X-ray selected QSOs, the bolometric luminosities are calculated from the X-ray luminosities, $L_{\mathrm{X}}(0.5 - 2\,\mathrm{keV})$, adopting a value of 33.3 as the bolometric correction factor (Stevens et al. 2005). The bolometric luminosities derived using the two different methods are on average in agreement with each other. This can be seen from the application of these two methods to the X-ray absorbed QSOs that also have B-band magnitudes.

3.2 Star Formation Rates

The star formation rates are estimated from the monochromatic luminosities at $60\,\mu\mathrm{m}$ ($L_{60\mu\mathrm{m}} = \nu L_{\nu}$ $(60\,\mu\mathrm{m})$),

$$\dot{M}_{\star} \approx 3.26\,M_{\odot}\,\mathrm{yr}^{-1}\frac{L_{60\,\mu\mathrm{m}}}{10^{10}L_{\odot}}. \tag{2}$$

The equation is obtained by the application of the conversion factors among the luminosities with different infrared wavelength coverage to the Kennicutt star formation rate law (Kennicutt 1998; see also Paper I for details). The star formation rate derived using Equation (2) is $\sim 50\%$ of that using the formula given in Paper I. This is because we found that the FIR luminosity between 40 and $120\,\mu\mathrm{m}$ in our case (for local IR QSOs) is roughly equal to, rather than a factor of two of, $L_{60\mu\mathrm{m}}$, as was assumed in Paper I (see also Martin et al. 2005). This downward revision is also consistent with the prescription given by Rowan-Robinson (2000). Therefore, we recalculated $\dot{M}_{\star}$ for IR QSOs using Equation (2). This does not, however, affect our main conclusions in Paper I (as the scatter around the mean relation is large).

For the $1.2\,\mathrm{mm}$ detected high-z QSOs, we estimated the rest-frame monochromatic luminosity at $60\,\mu\mathrm{m}$ from the observed flux density at $1.2\,\mathrm{mm}$ by assuming that the rest-frame FIR spectral energy distribution (SED) can be described by a greybody spectrum with a dust temperature of $41\,\mathrm{K}$ and a dust emissivity index (β) of 1.95. These parameters were derived by Priddey & McMahon (2001) by fitting the photometric measurements at submm and mm wavebands of several high-z ($z > 4$) quasars. Specifically, for QSOs with $1.2\,\mathrm{mm}$ observations, we apply the k-correction and obtain the rest-frame flux density at $1.2\,\mathrm{mm}/(1 + z)$; this step fixes the overall normalization of the greybody SED template, which can then be used to derive the rest-frame flux density at $60\,\mu\mathrm{m}$. The star formation rate is then obtained using Equation (2). For the X-ray selected and other $850\,\mu\mathrm{m}$ detected QSOs, the same method is applied at $850\,\mu\mathrm{m}$ instead of 1.2 mm.

In the previous studies, a rest-frame FIR SED with a dust temperature of $\sim 50\,\mathrm{K}$ and a dust emissivity index of $\beta \sim 1.5$ is often assumed (Omont et al. 2001; Carilli et al. 2001). Recent studies of the SEDs of more than ten high-z QSOs have given a best-fit temperature of $52 \pm 3\,\mathrm{K}$ and a dust emissivity index of $\beta = 1.5 \pm 0.1$, with individual dust temperatures ranging from 40 to $60\,\mathrm{K}$ (Beelen et al. 2006). If we adopt these dust parameter values, rather than the SED fitting results of Priddey & McMahon (2001), our

Table 3 Physical Parameters for 850 μm Detected QSOs

Name	Redshift	$S_{850\mu m}$	$\log(\frac{L_{bol}}{L_\odot})$	$\log(\frac{L_{60\mu m}}{L_\odot})$	$\log(\frac{\dot{M}_{acc}}{M_\odot\ yr^{-1}})$	$\log(\frac{\dot{M}_\star}{M_\odot\ yr^{-1}})$	$\log(\frac{\dot{M}_\star}{\dot{M}_{acc}})$
(1)	(2)	(3)	(4)	(5)	(6)	(7)	(8)
X-ray Absorbed QSOs[a]							
005734.78−272827.4	2.19	11.7±1.2	12.796	13.339	0.625	3.847	3.222
094144.51+385434.8	1.82	13.4±1.5	12.774	13.426	0.603	3.935	3.332
094356.53+164244.1	1.92	3.0±1.2	13.296	12.769	1.125	3.231	2.106
110431.75+355208.5	1.63	2.4±1.2	12.917	12.691	0.746	3.174	2.428
110742.05+723236.0	2.10	10.4±1.2	13.475	13.295	1.304	3.788	2.484
121803.82+470854.6	1.74	6.8±1.2	12.625	13.137	0.454	3.644	3.190
124913.86−055906.2	2.21	7.2±1.4	13.037	13.126	0.866	3.626	2.760
163308.57+570258.7	2.80	5.9±1.1	13.181	12.992	1.010	3.481	2.471
Isaak et al. (2002)							
PSSJ0452+0355	4.38	10.6±2.1	14.043	13.147	1.872	3.573	1.701
PSSJ0808+5215	4.44	17.4±2.8	14.484	13.360	2.313	3.748	1.435
PSSJ1048+4407	4.40	12.0±2.2	13.963	13.200	1.792	3.648	1.856
PSSJ1057+4555	4.12	19.2±2.8	14.760	13.417	2.589	3.734	1.145
PSSJ1248+3110	4.32	12.7±3.4	14.043	13.228	1.872	3.670	1.798
PSSJ1418+4449	4.32	10.4±2.3	14.443	13.141	2.272	3.444	1.172
PSSJ1646+5514	4.04	9.5±2.5	14.479	13.116	2.308	3.381	1.073
PSSJ2322+1944	4.11	22.5±2.5	14.240	13.487	2.069	3.945	1.876
McMahon et al. (1999)							
BR2237−0607	4.55	5.0±1.1	14.245	12.813	2.074	2.960	0.886
BRI0952−0115	4.43	14±2	14.084	13.266	1.913	3.709	1.796
BR1033−0327	4.50	7±2	14.045	12.962	1.874	3.332	1.458
BR1117−1329	3.96	13±1	14.238	13.257	2.067	3.672	1.605
BR1144−0723	4.14	7±2	14.000	12.978	1.829	3.367	1.538
BR1202−0725	4.69	42±2	14.407	13.732	2.236	4.203	1.967
BRI1335−0417	4.40	14±1	13.923	13.267	1.752	3.729	1.977
Priddey et al. (2003a) $z \gtrsim 2$							
LBQSB0018−0220	2.56	17.2±2.9	14.289	13.476	2.118	3.927	1.809
HSB0035+4405	2.71	9.4±2.8	14.334	13.201	2.163	3.575	1.412
HSB0211+1858	2.47	7.1±2.1	14.167	13.099	1.996	3.484	1.488
HSB0810+2554	1.50	7.6±1.8	14.562	13.198	2.391	3.475	1.084
HSB0943+3155	2.79	9.6±3.0	14.096	13.204	1.925	3.633	1.708
HSB1140+2711	2.63	8.6±2.6	14.372	13.169	2.201	3.517	1.316
HSB1141+4201	2.12	8.6±2.6	14.274	13.211	2.103	3.605	1.502
HSB1310+4308	2.60	10.0±2.8	14.131	13.237	1.960	3.667	1.707
HSB1337+2123	2.70	6.8±2.1	14.213	13.062	2.042	3.419	1.377
Priddey et al. (2003b) $z > 5$							
SDSSJ1306+0356	5.99	3.7±1.0	13.977	12.646	1.806	2.847	1.041
SDSSJ1044−0125	5.74	6.1±1.2	14.096	12.866	1.925	3.169	1.244
SDSSJ0756+4104	5.09	13.4±2.1	13.650	13.223	1.479	3.703	2.224
SDSSJ0338+0021	5.07	11.9±2.0	13.690	13.172	1.519	3.644	2.125

Notes: The columns have the same meanings as those in Table 1 but for detected QSOs at 850 μm.
[a] The name with prefix RXJ.

estimates of $L_{60\mu m}$ will be changed by only $\sim 20\% - 30\%$. However, when the individual dust temperature differences (40–60 K) are involved, the estimates will be changed by more than 0.5 dex for $\beta = 1.5 \pm 0.1$.

It is worth noting that the prescription we used here to obtain the star formation rate differs from that adopted by Carilli et al. (2001) and Omont et al. (2001, 2003). The latter would give a star formation rate that is several times lower than that from Equation (2). The differences arise from the different methods in deriving the IR or FIR luminosity, and different assumptions on the initial mass function, on stellar evolutionary theory and on the wavebands in which the absorbed starburst's total luminosity is re-emitted. As discussed by Kennicutt (1998), the star formation rates derived with different methods depend on a number
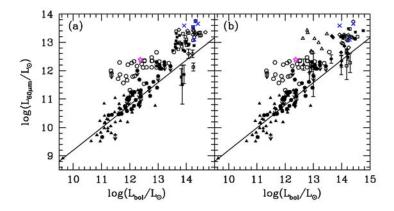
Fig. 1 Monochromatic luminosity at $60\,\mu\mathrm{m}$ vs. the bolometric luminosity of AGN for low-z objects and high-z QSOs observed (a) in mm and (b) in submm. In both panels: the open circles represent IR QSOs, filled circles and triangles represent PG QSOs and NLS1s, respectively; crosses are for the three QSOs with CO and/or HCN observations; the pentagram represents the distant ($z = 5.5$) optically faint ($M_{\mathrm{B}} \sim -24.2$) QSO (see text); the solid line is the best-fit regression line for the local PG QSOs and NLS1s obtained from survival analysis; the data points with error bars indicate the binned values for (sub)mm non-detected QSOs (see Sect. 4.1). In panel (a) open and filled squares represent QSOs taken from Omont et al. (2001) and Carilli et al. (2001), respectively; the diamonds represent QSOs from Omont et al. (2003). In panel (b) open triangles indicate the X-ray absorbed QSOs taken from Stevens et al. (2005); Open and filled squares represent objects from Priddey et al. (2003a) and Isaak et al. (2002), respectively; open and filled diamonds indicate the QSOs obtained from McMahon et al. (1999) and Priddey et al. (2003b). Stars with error bars are the binned data for X-ray unabsorbed, submm non-detected QSOs from Page et al. (2004).

of assumptions and are not precise; each method offers a useful means of estimating the star formation activity. For consistency, we shall use Equation (2) to estimate $\dot{M}_\star$ for objects in the local universe and at high redshift.

4 RESULTS AND DISCUSSION

4.1 (Sub)mm-Quiet and (Sub)mm-Loud QSOs

Figure 1a shows the rest-frame monochromatic luminosity at $60\,\mu\mathrm{m}$, $L_{60\mu\mathrm{m}}$, versus the bolometric luminosity associated with the central AGNs for all low-z sources and the $1.2\,\mathrm{mm}$ observed high-z QSOs. The regression line in Figure 1a is the best fit for low-z typical type 1 AGNs (PG QSOs and NLS1s). The close correlation between $L_{60\mu\mathrm{m}}$ and L_{bol} for low-z typical type 1 AGNs suggests that their FIR emissions are mainly powered by the central AGNs (see Paper I and Haas et al. 2003). It is clear from Figure 1a that all the high-z QSOs detected at $1.2\,\mathrm{mm}$ are located above the regression line just as the low-z IR QSOs.

The majority ($\sim 70\%$) of optically selected QSOs are, however, not detected at $1.2\,\mathrm{mm}$ above the 3σ level (e.g. Carilli et al. 2004; Momjian et al. 2005). We use the stacking method (Stevens et al. 2005) to obtain the mean value of the rest-frame $L_{60\mu\mathrm{m}}$ for the 95 QSOs that are not detected at $1.2\,\mathrm{mm}$. For each sample (see Sect. 2), we divide the redshift into bins of width of ≈ 0.5. The bolometric luminosity is simply the average of the objects in each bin. The $1.2\,\mathrm{mm}$ flux density is obtained as the mean of the sources in each bin weighted by their uncertainties. The rest-frame $L_{60\mu\mathrm{m}}$ is calculated in the way as described in Section 3.2, with the obtained mean flux densities and the mean bin redshift. The error bars of the binned data are calculated using error propagation by weighting the uncertainties of the observed flux densities at $1.2\,\mathrm{mm}$. The results from stacking are listed in Table 2 and plotted in Figure 1a. It is striking that the data points are all around the regression line inferred from the low-z typical type 1 AGNs.

A similar analysis was performed for high-z QSOs observed at $850\,\mu\mathrm{m}$ (instead of $1.2\,\mathrm{mm}$). These include QSOs selected optically and from X-ray (see Sect. 2). Figure 1b shows $L_{60\mu\mathrm{m}}$ vs. L_{bol} for all low-

Table 4 Binned Data for $850\,\mu$m Non-Detected QSOs (at 3σ level)

Number	mean redshift	weighted mean $S_{850\mu m}$	weighted mean $\log(\frac{L_{bol}}{L_\odot})$	weighted mean $\log(\frac{L_{60\mu m}}{L_\odot})$
		X-ray absorbed QSOs[a]		
10	1.289	0.772±0.354	12.652	12.210±0.199
		X-ray unabsorbed QSOs		
8	1.318	0.405±0.324	12.854	11.930±0.347
9	1.840	0.717±0.320	12.935	12.153±0.194
2	2.262	0.379±0.669	12.993	11.844±0.766
		Isaak et al. (2002)		
30	4.214	2.179±0.533	14.224	12.468±0.106
		McMahon et al. (1999)		
3	4.463	3.167±0.924	14.203	12.619±0.127
		Priddey et al. (2003a) $z \gtrsim 2$		
10	1.765	0.741±0.829	14.176	12.173±0.486
27	2.190	2.547±0.546	14.170	12.677±0.093
11	2.725	1.118±0.871	14.298	12.275±0.338
		Priddey et al. (2003b) $z > 5$		
6	5.100	2.078±0.726	13.627	12.413±0.152
3	5.577	1.800±0.884	13.992	12.339±0.213
1	6.280	1.300±1.000	13.979	12.189±0.334

Notes: The columns have the same meanings as those in Table 2 except that col. (3) is the weighted mean flux density at $850\,\mu$m. Some redshift bin widths are slightly different from 0.5 as the sample redshift range is slightly larger or smaller than 0.5. [a] One QSO at $z = 2.46$ with a flux density of -1.6 ± 1.2 at $850\,\mu$m was not included in the estimation because of its large redshift compared to the other non-detected QSOs (with $z \leq 1.5$).

z type 1 AGNs, IR QSOs, high-z submm detected QSOs and submm non-detected QSOs, which clearly indicates that all $850\,\mu$m non-detected QSOs except the X-ray absorbed ones are around the regression line derived from low-z type 1 AGNs. In contrast, all the $850\,\mu$m detected QSOs are above this regression line.

The similar behaviours of high-z QSOs observed at $850\,\mu$m by SCUBA and those observed at $1.2\,$mm by MAMBO in the relation of FIR luminosities to bolometric luminosities show that the difference between (sub)mm detected and non-detected QSOs may be real, rather than arising from the effects of instrument sensitivities. In fact, the samples used here were observed with different sensitivities, even for measurements made by the same instrument. For the $1.2\,$mm observations by MAMBO, the typical rms sensitivities vary from 0.5 to $1.4\,$mJy; while for the $850\,\mu$m observations by SCUBA, the sensitivities of the surveys vary from 1.5 to $3.3\,$mJy. In a word, the sensitivities vary by a factor of 2–3 for the different observations (Omont et al. 2001, 2003; Carilli et al. 2001; MaMchon et al. 1999; Issak et al. 2002). Observations with different sensitivities lead to significantly different weighted mean flux densities for the non-detected QSOs shown in Tables 2 and 4. Nevertheless, the positions of the (sub)mm non-detected QSOs are not strongly influenced by the sensitivities as they are all located around the regression line inferred for low-z typical QSOs. This suggests that the high-z (sub)mm non-detected QSOs may be analogues of typical QSOs seen locally and the FIR emission from these high-z objects are powered by AGNs, just as in the low-z typical QSOs. Of course, the high-z QSOs have higher accretion rates than their local counterparts.

On the other hand, for high-z QSOs detected at $1.2\,$mm and $850\,\mu$m, their rest-frame $L_{60\mu m}$ are all above the regression line for typical QSOs, implying that these objects are the analogues of low-z IR QSOs. For both the local and high-z samples, the excess FIR emission relative to the regression lines is probably provided by an additional energy source, namely massive starbursts in these objects.

Our conclusions are supported by the CO and/or HCN observations for three additional high-z QSOs (B1335$-$0417, B1202$-$0725 and J1148$+$5251, shown as crosses in Fig. 1a and 1b), which revealed massive molecular gas reservoirs in these three QSOs (10^{10} to $10^{11}\ M_\odot$, e.g., Carilli et al. 2002, 2004; Walter et al.
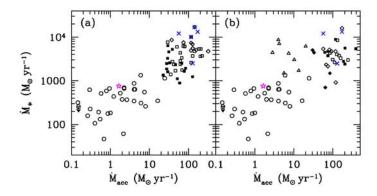
Fig. 2 Star formation rate ($\dot{M}_\star$) vs. the accretion rate ($\dot{M}_{acc}$) for local IR QSOs and high-z QSOs detected (a) in mm and (b) in sub-mm. The symbols are the same as in Fig. 1.

2003, 2004). Therefore, massive starbursts are occurring in the host spheroids of these objects and provide the dominant energy source for heating up the dust. In Figure 1a and 1b, the three QSOs are clearly located above the regression line for typical QSOs and they mix well with all the (sub)mm detected QSOs. In addition, two 1.2 mm detected QSOs (J140955.5+562827, Omont 2003; and PSS J2322+1944, Omont 2001, shown as crossed squares in Fig. 1a and 1b) have also been detected by CO observations. Note that only one (PSS J2322+1944) out of these five QSOs are magnified by gravitational lensing. In any case, lensing magnification should not be statistically important for most of our objects according to Vestergaard (2004).

In fact, from deep radio observations, it has already been suggested that the physics of submm-loud QSOs and submm-quiet QSOs may be different (Petric & Carilli 2004). Furthermore, the extended dust emission regions (larger than 1 kpc) of (sub)mm-loud QSOs rule out the central AGN heating model (Momjian et al. 2005 and references therein). Stevens et al. (2005) also argued that the submm emission of submm detected, X-ray absorbed QSOs is attributed to dust heated by hot young stars. The approach we adopt here is different but we reach the same conclusion – the high-z (sub)mm-loud QSOs are low-z analogues of IR QSOs and their ultraluminous/hyperluminous FIR emissions are mainly from dust heated by massive starbursts. As we show below, they are at a transition phase with rapid growth of black holes and their host spheroids.

4.2 Coeval Growth of Black Holes and Host Spheroids

Given that the ultraluminous/hyperluminous FIR emissions are mainly from dust heated by massive starbursts for both low-z IR QSOs and high-z (sub)mm-loud QSOs, we can estimate the star formation rates for these high-z (sub)mm-loud QSOs using the same method as for the low-z IR QSOs. The star formation rates are estimated from $L_{60\mu m}$, after subtracting the contribution from the central AGNs, on assuming the AGN contribution to $L_{60\mu m}$ for (sub)mm-loud QSOs follows the same regression line as typical QSOs shown as the solid line in Figure 1.

Figure 2 shows the star formation rate versus the accretion rate for IR QSOs and high-z (sub)mm-loud QSOs. It is obvious from Figure 2 that for QSOs with larger accretion rates and hence higher bolometric luminosities, the star formation rates are also higher. This trend directly indicates that the more massive galaxies build their spheroid stellar masses and central black holes faster than the less massive ones, and hence the most massive galaxies host the most luminous QSOs in their centers. Although this trend has been noticed in Paper I, the combination of high-z (sub)mm-loud QSOs with the local IR QSOs provides a much larger dynamical range for studying the relation between $\dot{M}_\star$ and $\dot{M}_{acc}$ than either sample alone. This is appropriate because the underlying physics of QSOs at low and high redshift may be similar (Fan et al. 2004; Vestergaard 2004 and references therein; see also below). Thus we can extend the dynamic
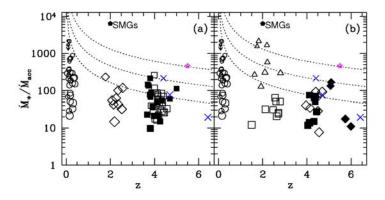
Fig. 3 Ratio of $\dot{M}_\star$ and $\dot{M}_{\rm acc}$ vs. redshift for local IR QSOs, (a) high-z mm detected QSOs and (b) high-z submm detected QSOs. The symbols are the same as in Fig. 1. The sizes of the data points indicate their bolometric luminosities associated with AGNs. The dotted lines are for three flux limits corresponding to three bolometric luminosities, $10^{11} L_\odot$, $10^{12} L_\odot$ and $10^{13} L_\odot$ (from top to bottom), at redshift 2.0. For each curve we assume the relation between the star formation rate and the accretion rate by simply fitting a regression line to the data points in Fig. 2a using survival analysis.

range in the bolometric luminosity by combining together low- and high-redshift samples. In contrast, this trend was not found based on high-z (sub)mm observed QSOs alone (e.g. Isaak et al. 2002; Omont et al. 2003) because of the limited dynamical range and large scatters involved. In addition, the inclusion of both (sub)mm-loud and (sub)mm-quiet QSOs in the previous analyses has also obscured the trend as these two types of objects may be at physically different evolutionary stages (see below).

As can be seen from Figure 2a and 2b, for a fixed $\dot{M}_{\rm acc}$, there is roughly a 1 dex scatter in $\dot{M}_\star$. The large scatter may be partly due to the calibration errors in Equation (2), and the differences in the FIR SED of the QSOs. Nevertheless, it is quite likely that $\dot{M}_\star/\dot{M}_{\rm acc}$ does vary from object to object. Therefore, it is worth investigating how the $\dot{M}_\star/\dot{M}_{\rm acc}$ changes with the redshifts and bolometric luminosities of QSOs.

Figure 3 shows $\dot{M}_\star/\dot{M}_{\rm acc}$ versus redshift for low-z IR QSOs and high-z (sub)mm-loud QSOs. The sizes of the data points are scaled by their accretion rates, i.e., by their bolometric luminosities. It is obvious from Figure 3 that there is an absence of QSOs with large $\dot{M}_\star/\dot{M}_{\rm acc}$ at higher redshift. This may be caused by the Malmquist bias – for a flux-limited sample, as the redshift (distance) increases, more luminous objects are preferentially selected. In our case objects with lower accretion rates could have been missed at high z, although the samples we used here are not strictly flux-limited (most of our QSOs are optically luminous QSOs with $M_{\rm B} < -27.0$). To illustrate the effect of the Malmquist bias quantitatively, we plot three dotted curves in Figure 3a and 3b corresponding to bolometric luminosities of $10^{11} L_\odot$, $10^{12} L_\odot$ and $10^{13} L_\odot$ at redshift 2, which covers the whole range of bolometric luminosity of low-z IR QSOs. For each curve, we assume the relation between the star formation rate and the accretion rate by simply fitting a regression line to the data points in Figure 2a using survival analysis (Isobe et al. 1986). In an optically selected flux-limited sample, the objects above these dotted lines will be missed during the observations with the flux limits assumed above. From the shapes of these dotted lines, we can see that the higher ratios at lower redshift can be reproduced by the Malmquist bias, so the lack of high $\dot{M}_\star/\dot{M}_{\rm acc}$ QSOs at high z may not be real.

There is a well-studied high-z ($z = 5.5$) optically faint ($M_{\rm B} \sim -24.2$) QSO – RDJ030117+002025 (Stern et al. 2000; Bertoldi & Cox 2002; Staguhn et al. 2005) to test the above argument. This object is represented by the pentagram in all three figures. From its location in Figures 1–3, we can see that its behavior is similar to the low-z IR QSOs. This suggests that at least some distant optically faint QSOs have similar properties to low-z IR QSOs, and verifies the combination of low-z IR QSOs and high-z (sub)mm-loud QSOs in Figure 2. However, more (sub)mm observations of high-z optically faint QSOs are needed to firmly establish this idea.

On the other hand, it can be seen from Figure 3 that the $\dot{M}_\star/\dot{M}_{\mathrm{acc}}$ of the low-z IR QSOs and high-z (sub)mm-loud QSOs both span a broad range and that there is a clear trend that as the bolometric luminosity (indicated by the size of data points) increases, $\dot{M}_\star/\dot{M}_{\mathrm{acc}}$ decreases. Thus the behavior of the relative growth of host spheroids and their central black holes is correlated with the power of the QSOs – the optically more luminous QSOs correspond to a phase of higher accretion rates and relatively low star formation rates, which results in the absence of optically luminous QSOs (shown as symbols with larger sizes in Fig. 3a and 3b) with large $\dot{M}_\star/\dot{M}_{\mathrm{acc}}$. This trend is consistent with the prediction by the simulations of Cattaneo et al. (2005, fig. 11).

In Figure 3 we also indicate the mean position of the SMGs (the pentagon) using their data in the Chandra Deep Field North with deep Keck spectroscopic data in Alexander et al. (2005b). The mean position of the SMGs is obtained using the mean redshift and mean $\dot{M}_\star/\dot{M}_{\mathrm{acc}}$ in the Alexander et al. (2005b) sample. It is clear from Figure 3 that the SMGs are located above the FIR ultraluminous/hyperluminous QSOs.

The locations of SMGs and FIR ultraluminous/hyperluminous QSOs in Figure 3 suggest a possible evolutionary picture from top to bottom in terms of $\dot{M}_\star/\dot{M}_{\mathrm{acc}}$. The SMGs represent prodigious starbursts triggered by interactions and major mergers as revealed by Hubble Space Telescope images in the rest-frame ultra-violet wavebands (Conselice et al. 2003; Smail et al. 2004). Although $> 38^{+12}_{-10}\%$ SMGs host AGNs, the dominant rest-frame FIR energy output for most of them is still from starbursts (Alexander et al. 2005b) and this population is expected to be at a pre-QSO phase, during which the central black holes grow more slowly compared with their spheroid hosts. As the gas falls toward the centers of galaxies, the accretion rate increases while the massive starbursts continue, thus undergoing a phase of simultaneous growth of central black holes and their spheroids. This phase of simultaneous growth may be quite short (10^7 to 10^8 years) if the (sub)mm-detected QSO fraction (20%–30%) can be interpreted as the relative duty cycle (e.g. Carilli et al. 2004). The very high star formation rates and accretion rates in this phase lead to a rapid increase of the masses of the central black holes and spheroids. As the black hole mass increases, the central AGN becomes more energetic, and the AGN feedback process may heat up and blow away the surrounding gas and dust, leading to a decrease in the star formation rate and in $\dot{M}_\star/\dot{M}_{\mathrm{acc}}$. Eventually, it enters the typical QSO phase with a high accretion rate and a low star formation rate. QSOs at this stage are located at the bottom of Figure 3.

The picture described above corresponds well with the evolutionary sequence for low-z gas-rich major mergers, from ultraluminous IR galaxies to IR QSOs (or FIR luminous Seyfert 1s, Sanders et al. 1988a,b), and finally to L^* elliptical galaxies. The difference is that high-z SMGs have more gas and may evolve into giant elliptical galaxies. While not every single object may fit in this picture, e.g., the high-z QSOs with large black hole mass and relatively low host dynamical mass may have a different evolutionary path, many ultraluminous IR galaxies (at low redshift) and SMGs (at high redshift) will evolve into L^* and giant ellipticals respectively along this path.

5 SUMMARY

In this paper we have examined the properties of high-z QSOs samples observed at 1.2 mm, $850\,\mu$m or with CO and/or HCN observations. The redshift of these objects spans from 1.0 to 6.42. Applying the same criteria established for local type 1 AGNs (Hao et al. 2005), we found that statistically, the (sub)mm detected and non-detected high-z QSOs are analogues of local IR QSOs and typical type 1 AGNs, respectively. We postulated that the underlying physics of (sub)mm detected and non-detected high-z QSOs may be different, and that they correspond to different phases in the interplay between the formations of the AGNs and spheroids.

For (sub)mm-loud QSOs, the FIR ultraluminous/hyperluminous emissions are from dust heated predominantly by starbursts. By combining low-z IR QSOs and high-z (sub)mm-loud QSOs, we found a clear trend that the higher the accretion rate, the larger the star formation rate. It directly indicates that the most massive galaxies host the most luminous QSOs at their centers. We also found that the relative growth of black holes and their host spheroids depends on the intensity of QSO activities, in qualitative agreement with theoretical expectations. We also compared the properties of SMGs, ultraluminous or hyperluminous FIR QSOs and typical QSOs, and constructed a possible evolution scenario among these objects. Clearly, substantial growth of black holes and their host spheroids can occur in these objects. Future studies of

these objects are therefore important for understanding how the formations of spheroids and AGNs are inter-connected and how the $M_{\rm BH}$-$M_\star$ relation arises.

References

Adams F. C., Graff D. S., Richstone D. O., 2001, ApJ, 551, L31

Alexander D. M., Smail I., Bauer F. E. et al., 2005, Nature, 434, 738

Alexander D. M., Bauer F. E., Chapman S. C. et al., 2005, ApJ, 632, 736 (2005b)

Balberg S., Shapiro S. L., 2002, Phys. Rev. Lett., 88, 101301

Bertoldi F., Carilli C. L., Cox P. et al., 2003, A&A, 406, L55

Bertoldi F., Cox P., 2002, A&A, 384, L11

Borys C., Smail I., Chapman S. C. et al., 2005, ApJ, 635, 853

Burkert A., Silk J., 2001, ApJ, 554, L151

Carilli C. L., Bertoldi F., Rupen M. P. et al., 2001, ApJ, 555, 625

Carilli C. L., Kohno K., Kawabe R. et al., 2002, AJ, 123, 1838

Carilli C. L., Bertoldi F., Walter F. et al., 2004, in Proc. Multiwavelength AGN Surveys, eds. R. Maiolino, R. Mujica, World Scientific Publishing Company, Singapore, p.115

Carilli C. L., Solomon P., Vanden Bout P. et al., 2005, ApJ, 618, 586

Cattaneo A., Blaizot J., Devriendt J. et al., 2005, MNRAS, 364, 407

Chapman S. C., Smail I., Windhorst R. et al., 2004, ApJ, 611, 732

Conselice C. J., Chapman S. C., Windhorst R. A., 2003, ApJ, 596, L5

Di Matteo T., Springel V., Hernquist L., 2005, Nature, 433, 604

Downes D., Solomon P. M., 1998, ApJ, 507, 615

Fan X., Hennawi J. F., Richards G. T. et al., 2004, AJ, 128, 515

Ferrarese L., Merritt D., 2000, ApJ, 539, L9

Haas M., Klaas U., Müller S. A. H. et al., 2003, A&A, 402, 87

Haehnelt M., Kauffmann G., 2000, MNRAS, 318, L35

Hao C. N., Xia X. Y., Mao S., Wu H., Deng Z. G., 2005, ApJ, 625, 78

Heckman T. M., Kauffmann G., Brinchmann J. et al., 2004, ApJ, 613, 109

Isaak K. G., Chandler C. J., Carilli C. L., 2004, MNRAS, 348, 1035

Isaak K. G., Priddey R. S., McMahon R. G. et al., 2002, MNRAS, 239, 149

Isobe T., Feigelson E. D., Nelson P. I., 1986, ApJ, 306, 490

Kennicutt R. C., 1998, ARA&A, 36, 189

Kim D.-C., Veilleux S., Sanders D. B., 1998, ApJ, 508, 627

Kormendy J., Gebhardt K., 2001, In: AIP Conf. Proc. 586, Relativistic Astrophysics, H. Martel, J.C. Wheeler, eds, New York: AIP, 363

Kreysa E., Gemuend, H., Gromke J. et al., 1998, Proc. SPIE, 3357, 319

Laor A., 1998, ApJ, 505, L83

Magorrian J., Tremaine S., Richstone D. et al., 1998, AJ, 115, 2285

Martin D. C., Seibert M., Buat V. et al., 2005, ApJ, 619, L59

McMahon R. G., Priddey R. S., Omont A. et al., 1999, MNRAS, 309, L1

Momjian E., Carilli C. L., Petric A. O., 2005, AJ, 129, 1809

Omont A., Beelen A., Bertoldi F. et al., 2003, A&A, 398, 857

Omont A., Cox P., Bertoldi F. et al., 2001, A&A, 374, 371

Omont A., McMahon R. G., Cox P. et al., 1996, A&A, 315, 1

Page M. J., Stevens J. A., Ivison R. J. et al., 2004, ApJ, 611, L85

Petric A. O., Carilli C. L., 2004, IAUS, 222, 535

Priddey R. S., McMahon R. G., 2001, MNRAS, 324, L17

Priddey R. S., Isaak K. G., McMahon R. G. et al., 2003, MNRAS, 339, 1183 (2003a)

Priddey R. S., Isaak K. G., McMahon R. G. et al., 2003, MNRAS, 344, L74 (2003b)

Robson I., Priddey R. S., Isaak K. G., McMahon R. G., 2004, MNRAS, 351, L29

Rowan-Robinson M., 2000, MNRAS, 316, 885

Sanders D. B., Soifer B. T., Elias J. H. et al., 1988, ApJ, 325, 74 (1988a)

Sanders D. B., Soifer B. T., Elias J. H. et al., 1988, ApJ, 328, L35 (1988b)

Shields G. A., Gebhardt K., Salviander S. et al., 2003, ApJ, 583, 124

Shields G. A., Menezes K. L., Massart C. A., Vanden Bout P., 2006, ApJ, 641, 683

Silk J., Rees M. J., 1998, A&A, 331, L1

Smail I., Chapman S. C., Blain A. W., Ivison R. J., 2004, ApJ, 616, 71

Springel V., Di Matteo T., Hernquist L., 2005, MNRAS, 361, 776

Staguhn J. G., Stern D., Benford D. J. et al., 2005, ApJ, 629, 633

Stern D., Spinrad H., Eisenhardt P. et al., 2000, ApJ, 533, L75

Stevens J. A., Page M. J., Ivison R. J. et al., 2005, MNRAS, 360, 610

Tacconi L. J., Neri R., Chapman S. C. et al., 2006, ApJ, 640, 228

Tremaine S., Gebhardt K., Bender R. et al., 2002, ApJ, 574, 740

Treu T., Malkan M. A., Blandford R. D., 2004, ApJ, 615, L97

Vestergaard M., 2004, ApJ, 601, 676

Walter F., Bertoldi F., Carilli C. et al., 2003, Nature, 424, 406

Walter F., Carilli C., Bertoldi F. et al., 2004, ApJ, 615, L17

Zheng X. Z., Xia X. Y., Mao S. et al., 2002, AJ, 124, 18